Laser and Particle Beams (2016), *34*, 115–122.

doi:10.1017/S0263034615001032

Electron acceleration at grazing incidence of a subpicosecond intense laser pulse onto a plane solid target

N. E. ANDREEV, L. P. PUGACHEV, M. E. POVARNITSYN, AND P. R. LEVASHOV
Joint Institute for High Temperatures RAS, 13 Izhorskaya str., Bldg. 2, Moscow 125412, Russia
(RECEIVED 15 October 2015; ACCEPTED 4 November 2015)

Abstract

Generation of hot electrons at grazing incidence of a subpicosecond relativistic-intense laser pulse onto a plane solid target is analyzed for the parameters of petawatt class laser systems. We study preplasma formation on the surface of solid aluminum targets produced by laser prepulses with a different time structure. For modeling of the preplasma dynamics, we use a wide-range two-temperature hydrodynamic model. As a result of simulations, the preplasma expansion under the action of the laser prepulse and the plasma density profiles for different contrast ratios of the nanosecond pedestal are found. These density profiles are used as the initial density distributions in three-dimensional particle-in-cell simulations of electron acceleration by the main *P*-polarized laser pulse. Results of modeling demonstrate a substantial increase of the characteristic energy and number of accelerated electrons for the grazing incidence of a subpicosecond intense laser pulse in comparison with the ponderomotive scaling of laser–target interaction.

Keywords: Electron acceleration; Grazing laser pulse incidence; Laser–matter interaction; Particle-in-cell method

1. INTRODUCTION

For relativistic intensities of a main subpicosecond pulse, even high-contrast beams can produce plasma on a target surface due to a long nanosecond and picosecond prepulses impact, which results in target surface modifications before the main pulse action, and influences the subpicosecond pulse interaction with the target extremely (Povarnitsyn *et al*., 2012*b*, 2013; Esirkepov *et al*., 2014). In this paper, the generation of hot electrons at grazing incidence of a subpicosecond intense laser pulse onto a plane solid target is analyzed for the parameters of the petawatt high-energy laser for heavy ion experiments (PHELIX) (Bagnoud *et al*., 2010; Wagner *et al*., 2014*a*) using three-dimensional (3D) particle-in-cell (PIC) modeling (Pukhov, 1999) and a wide-range hydro modeling (Povarnitsyn *et al*., 2012*a*) of the preplasma expansion under the action of the laser prepulse. Elaboration of wide-range models of the laser–matter interaction is necessary for planning and interpretation of experiments carried out in view of different applications aimed for the development of secondary sources of high energy particles and hard radiation (Morace *et al*., 2014; Brabetz *et al*., 2015; Rusby *et al*., 2015; Vaisseau *et al*., 2015). Surface acceleration and transport of energetic electrons in intense laser–matter interactions at the grazing incidence were investigated experimentally for femtosecond laser pulses of hundreds mJ energy in (Wang *et al*., 2013; Mao *et al*., 2015) and for hundred joule subpicosecond laser pulses of the laser system PHELIX in paper (Gray *et al*., 2011).

For different laser systems the contrast of a nanosecond prepulse of amplified spontaneous emission (ASE) can vary within wide limits from 10^{-6} to 10^{-12} and higher, when plasma mirror focusing is used. The normal ASE contrast (or pedestal) is between 10^{-6} and 10^{-7}, if no special measures are taken. A typical time structure of the petawatt class laser pulse is shown in Figure 4 of (Wagner *et al*., 2014*b*), where the pulse shape of the PHELIX laser at the first harmonic, $\lambda_0 = 1.053$ μm, is shown for different parameters of the contrast boosting module. For simulation of the laser–matter interaction at non-relativistic prepulse intensities, we have elaborated and used the two-temperature single-fluid radiation hydrodynamic model (Povarnitsyn *et al*., 2012*a*, 2013). This wide-range model describes laser energy absorption, electron–ion coupling and two-temperature effects, radiation transport, thermodynamic properties of materials, and ionization from normal conditions at room temperature to weakly non-ideal high-temperature plasma. Using the model we have studied pump-probe experiments (Povarnitsyn *et al*., 2012*a*) as well as the action of a nanosecond prepulse on thin films (Povarnitsyn *et al*., 2012*b*, 2013). As

Address correspondence and reprint request to: M. E. Povarnitsyn, Joint Institute for High Temperatures RAS, 13 Izhorskaya str., Bldg. 2, Moscow 125412, Russia. E-mail: povar@ihed.ras.ru

opposed to the Radiative Arbitrary Lagrangian–Eulerian Fluid dynamics in two dimensions code (Ortner *et al.*, 2015), in our model, the laser absorption is described using the wave equation for the laser pulse electric field.

This paper is organized as follows. Preplasma formation under the action of different contrasts prepulses is modeled and described in Section 2. The results of 3D PIC modeling of the electron acceleration by the main subpicosecond relativistic-intense laser pulse (with parameters typical for the PHELIX laser system at the first harmonic, $\lambda_0 = 1.053$ μm) in the plasma produced by the prepulse are presented in Section 3. Discussion and conclusion are summarized in Section 4.

2. PREPLASMA FORMATION UNDER THE ACTION OF DIFFERENT PREPULSE CONTRASTS

To describe plasma corona formation under the action of different intensity prepulses, the 1D version (Povarnitsyn *et al.*, 2013) of the HELIO2D code (Andreev *et al.*, 2015) was used, which takes into account 1D hydrodynamic motion of matter, laser energy absorption, two-temperature non-equilibrium states for electron and ion subsystems, electron thermal conductivity, and radiation transport in diffusion approximation. The evolution of material parameters is described using the conservation of mass, momentum, and energy of electron and ion subsystems in a single-fluid two-temperature Lagrangian form.

2.1. Picosecond laser prepulse

While a nanosecond ASE prepulse can be substantially reduced by different measures, the prepulse emission on the timescale of a few tens of picoseconds is practically always present [see Fig. 4 of (Wagner *et al.*, 2014*b*)]. The importance of the multi-picosecond target dynamics in relativistic laser–matter interactions was recently emphasized in a publication (Schollmeier *et al.*, 2015), where it was shown that inclusion of realistic temporal laser pulse profiles in modeling is necessary for the correct description of the laser energy conversion to hot electrons.

In our modeling of the plasma formation, we analyzed firstly the bulk Al target heating by the PHELIX picosecond prepulse only during the time interval $(-100, -5)$ ps, as shown in Figure 1 for high contrast level $\sim 10^{-10}$ at time less than -100 ps (zero time moment corresponds to the maximum of the laser pulse intensity).

The electron density distribution at $t = -5$ ps is shown in Figure 2 for the *P*-polarized laser pulse with the angle of incidence 80° and maximum intensity 4×10^{19} W/cm^2. For electron densities less than, or about the density of the reflection point y_r, the density profile can be well approximated by the rarefaction wave exponent with a characteristic scale length $L_r = 1.8$ μm:

$$n_e(y) = n_{e,r} \exp[(y - y_r)/L_r], \quad (1)$$

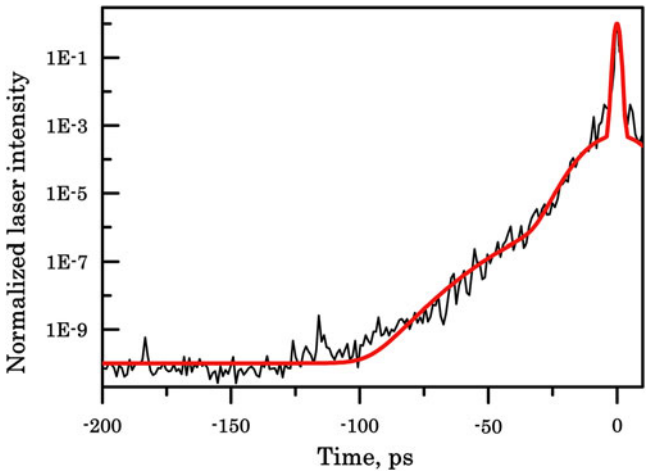

Fig. 1. Time structure of the PHELIX laser pulse at the first harmonic, $\lambda_0 = 1.053$ μm, in a subnanosecond domain for high contrast level $\sim 10^{-10}$ at time less than -100 ps. Solid (black) curve presents the cross-correlation measurement, dashed (red) curve is an approximation used in simulations. Laser intensity is normalized to the maximum of the main pulse intensity.

where $n_{e,r} \equiv n_e(y_r) = n_{cr} \cos^2\theta \approx 0.03 \times n_{cr} \approx 3 \times 10^{19}$cm^{-3} for the angle of incidence $\theta = 80°$ and the laser wavelength $\lambda_0 = 1.053$ μm ($n_{cr} = \omega_0^2 m_e / 4\pi e^2$ is the critical density for the laser frequency $\omega_0 = 2\pi c/\lambda_0$). Here and hereinafter the electron plasma density is in the centimetre–gram–second system of units, while the scale length is in micrometers. The sum of distribution Eq. (1) and two high gradient exponential density profiles with the scale lengths of 0.45 and 0.05 μm at the densities 10^{22} and 10^{23} cm^{-3}, respectively, reproduces quite well the total density profile of plasma corona obtained in simulation (see empty green circles in Fig. 2).

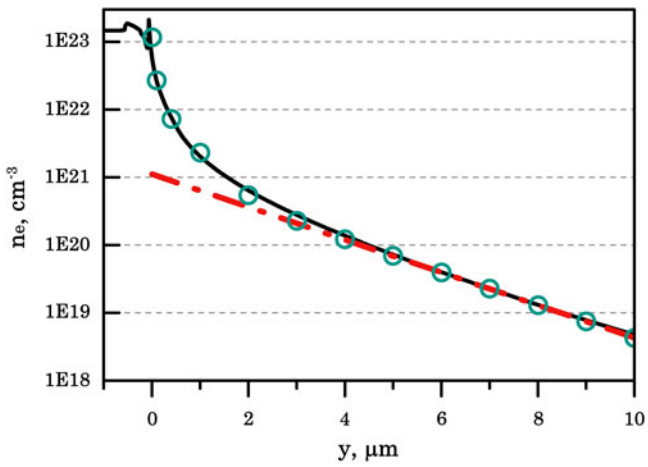

Fig. 2. The electron density distribution at $t = -5$ ps (before the main pulse) by the action of the picosecond prepulse only. Thick (black) curve is the results of modeling; dash-dot (red) curve is the rarefaction wave exponent Eq. (1); empty (green) circles show a three-exponent approximation. Laser pulse parameters are indicated in the text.

https://doi.org/10.1017/S0263034615001032 Published online by Cambridge University Press

This three-exponential electron density profile of the plasma produced by the prepulse was used for modeling of the electron acceleration by the main picosecond laser pulse with a high contrast nanosecond ASE pedestal (of the level $\leq 10^{-11}$ when its influence can be neglected and only the picosecond prepulse can produce plasma before the main pulse action).

2.2. Nanosecond ASE pedestals

The influence of the 1 ns ASE pedestal (which acts before −100 ps, see Fig. 1) on the preplasma electron density distribution was investigated for the pedestal intensities in the range of 10^9–4×10^{11} W/cm^2 for the same main laser pulse parameters (*P*-polarization, angle of incidence 80°, and maximum intensity 4×10^{19} W/cm^2) that corresponds to the pedestal contrast levels in the range 2.5×10^{-11}–10^{-8}. All over these pedestal intensities, for the electron densities less and about the reflection point y_r [$n_e(y_r) = n_{cr} \cos^2 \theta \approx 3 \times 10^{19}$ cm^{-3}] the density profile can be well approximated by the rarefaction wave exponent (1) with the characteristic scale length L_r in the range of 2–40 μm (see Fig. 3). The reflection point position y_r demonstrates the plasma propagation as a function of the pedestal intensity (see Fig. 3).

These modeling results evidently show that even at a rather high contrast of the laser pulse pedestal of the order of 10^{-10} and a nanosecond duration, the characteristic scale length of the produced preplasma can be increased two times (L_r = 3.6 μm) before the main short laser pulse action. For a lower contrast of the laser pulse pedestal in the range 10^{-9}–10^{-8} (and also for smaller angles of laser incidence), the characteristic scale length of the prepulse produced plasma can increase substantially and reach tens of microns as shown in Figure 3.

The exponential electron density profiles of the prepulse produced plasma with a characteristic scale length from $L_r \approx 2 \div 4$ to 30 μm near the reflection point were used for PIC modeling of the electron acceleration by the main subpicosecond laser pulse with different contrast levels of the nanosecond ASE pedestal.

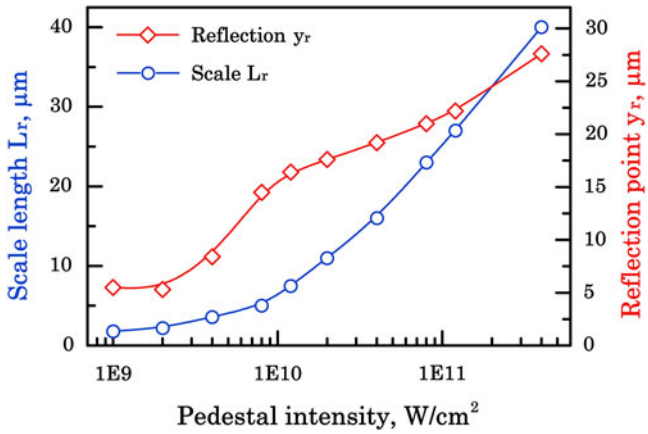

Fig. 3. The characteristic scale length of the prepulse produced plasma L_r at the reflection point at $t = -5$ ps (before the main pulse) taking into account ASE pedestal of the length 1 ns, as a function of the laser pulse pedestal intensity – solid (blue) curve with empty circles. Circles are the result of approximation (1) of the plasma expansion, the line is the B-spline interpolation of the points. *P*-polarized laser pulse with the angle of incidence 80° is considered. The reflection point position corresponding to $0.03 \times n_{cr}$ – solid (red) curve with empty diamonds.

3. LASER-PLASMA ELECTRON ACCELERATION

PIC simulations were carried out with the 3D PIC code Virtual Laser Plasma Laboratory (Pukhov, 1999). The geometry of interaction is shown in Figure 4.

The density profiles obtained by the wide-range hydro modeling of the preplasma expansion under the action of the laser prepulse were attached at $y \geq 0$ to the homogeneous plasma slab with the electron density of $100 \times n_{cr}$ and thickness of 5 μm over the *OY*-axis [$y \in (-5, 0)$ μm, see Fig. 4]. The simulation box had the sizes of 400 μm along the *OX*-axis and 80 μm along the *OZ*-axis. The size along the *OY*-axis was varied from 90 to 230 μm for various preplasma density profiles to get the reflection point y_r inside the simulation box far enough from the boundaries. Cells with sizes $0.05 \times 0.5 \times 0.5$ μm^3 and four particles per cell for the electrons were used together with immobile ions which produced neutralizing background.

The main *P*-polarized laser pulse with the Gaussian envelope in time and space, $\lambda_0 = 1$ μm, the full width at half maximum (FWHM) pulse duration 400 fs and energy 120 J was focused in the FWHM spot size of 25 μm with the angle of incidence 80° and maximum intensity 4×10^{19} W/cm^2. Initially, at $t = 0$, the center of the laser pulse was far enough from the target at $x_0 = -200$ μm, $z_0 = 40$ μm, and y_0 was varied so that the pulse reached the reflection point y_r at the middle of the *x*-length of the simulation box (at $x \approx 200$ μm).

Figure 5 shows the energy spectra of accelerated electrons for the initial density scale lengths L_r = 1.8 and 3.6 μm, typical for the contrast of the laser pulse nanosecond pedestal

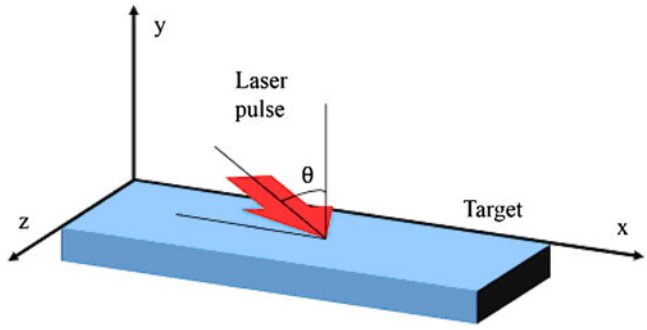

Fig. 4. Geometry used in 3D PIC simulations: $y = 0$ corresponds to the initial position of the solid target surface. The laser pulse is incident on plasma, which is spread out to $y > 0$ with an exponential electron density profile produced by the laser prepulse (see Figs 2 and 3).

https://doi.org/10.1017/S0263034615001032 Published online by Cambridge University Press

from 10^{-11} to 10^{-10}. The spectrum with a hot temperature $T_h = 2.3$ MeV predicted by the ponderomotive electron energy at a peak laser intensity (Wilks *et al.*, 1992) is shown also by the dotted line in Figure 5 for the coefficient of transformation of the laser energy to the hot electrons energy $\eta = 0.07$. With the increase in L_r within a few micrometers the number of accelerated electrons drops for the energies higher than 30 MeV.

The lower contrast nanosecond ASE pedestal of the laser pulse can create longer density scales of the preplasma with $L_r \geq 10$ μm (see Fig. 3). In this case, the accelerating mechanism changes and the maximum energy of accelerated electrons can reach hundreds of MeV. The dependences of spectra of accelerated electrons on the laser pulse polarization and the angle of incidence are illustrated in Figure 6 for the fixed initial density scale length $L_r = 10$ μm.

With the increase of the characteristic density scale length, the maximum energy of accelerated electrons grows up to about 300 MeV for the density scale length $L_r = 20$ μm (at the expense of some decrease of the number of particles for the energies less than 50 MeV in comparison with a longer density scale length 30 μm, see Fig. 7).

Figure 8 illustrates qualitatively different angular distributions of accelerated electrons for different scale lengths formed by different contrast laser prepulses. For the preplasma scale length $L_r = 20$ μm, which can be produced by the nanosecond ASE pedestal of an intensity about 10^{11} W/cm^2 (see Fig. 3), accelerated electrons propagate at a small angle to the target surface, and the width of the angular distribution decreases for higher electron energies (upper plots of Fig. 8). While for a lower level of the laser pulse nanosecond ASE pedestal (of intensity less than 10^9 W/cm^2, when the preplasma scale length $L_r = 1.8$ μm), there are two jets of accelerated electrons propagating outward and inside the target with the angle (relative to the target surface) about the angle of propagation of the reflected laser pulse (lower plots of Fig. 8).

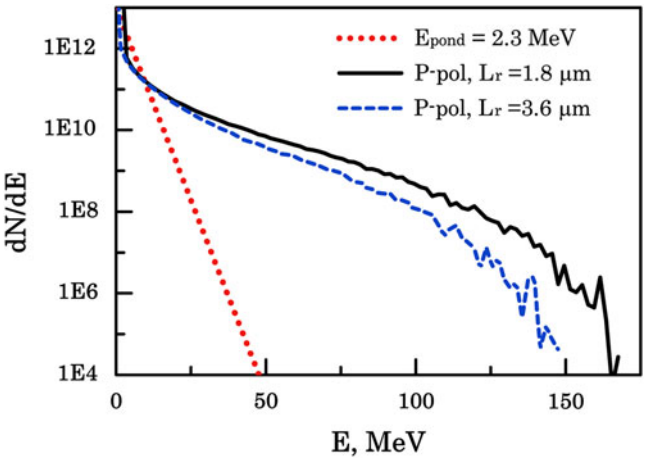

Fig. 5. Electron energy spectra for the initial density scale length $L_r = 1.8$ μm – solid (black) curve and $L_r = 3.6$ μm – dashed (blue) curve. Dotted (red) curve shows the spectrum for a hot temperature $T_h = 2.3$ MeV predicted by the ponderomotive electron energy.

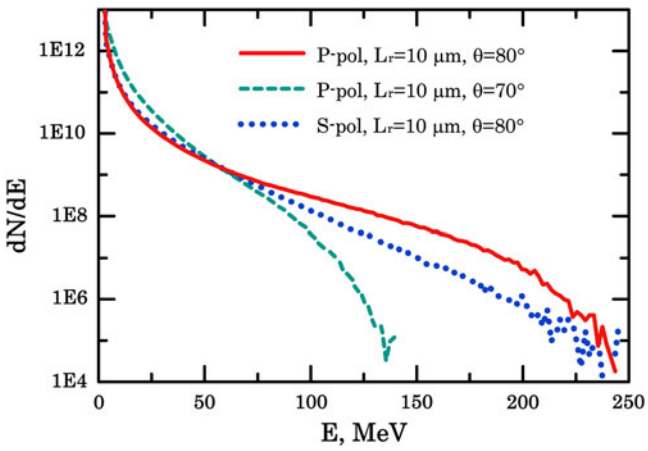

Fig. 6. Electron energy spectra for the initial density scale length $L_r = 10$ μm at different laser pulse polarizations and angles of incidence. Solid (red) and dashed (green) curves are for the *P*-polarization, $\theta = 80$ and 70°, respectively; dotted (blue) curve shows the spectrum for the *S*-polarization, $\theta = 80°$.

4. DISCUSSION AND CONCLUSIONS

Different energy spectra and angle distributions of hot electrons at ten times different preplasma scale lengths $L_r = 1.8$ and 20 μm (see Figs 5, 7, and 8) indicate different mechanisms of the electron acceleration in the plasma corona. In the case of sharp (short scale length) plasma density gradients, produced quasi-static electric and magnetic fields are significant for generation and transport of high energy electrons along the surface of a solid target irradiated by high power laser pulses. The importance of quasi-static fields in the electron acceleration by a self-channeled relativistic-intense laser pulse was shown in paper (Pukhov *et al.*, 1999). The mechanism and conditions for the formation of quasi-static surface fields at oblique incidence of a short intense laser pulse onto a solid target with a short scale

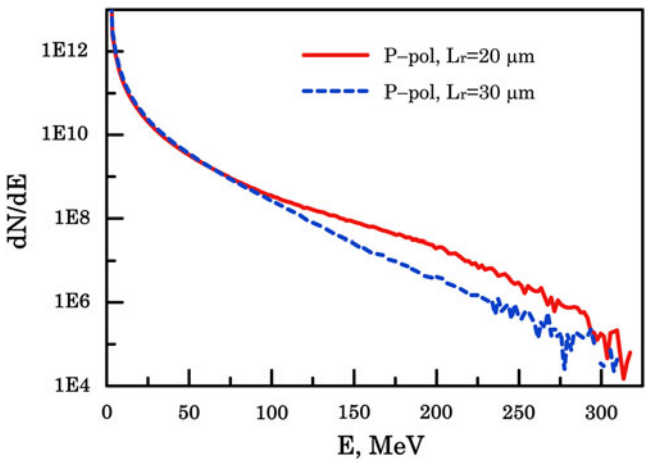

Fig. 7. Electron energy spectra for the *P*-polarized laser pulse with the angle of incidence $\theta = 80$ and different initial density scale lengths: Solid (red) curve for $L_r = 20$ μm and dashed (blue) curve for $L_r = 30$ μm.

https://doi.org/10.1017/S0263034615001032 Published online by Cambridge University Press

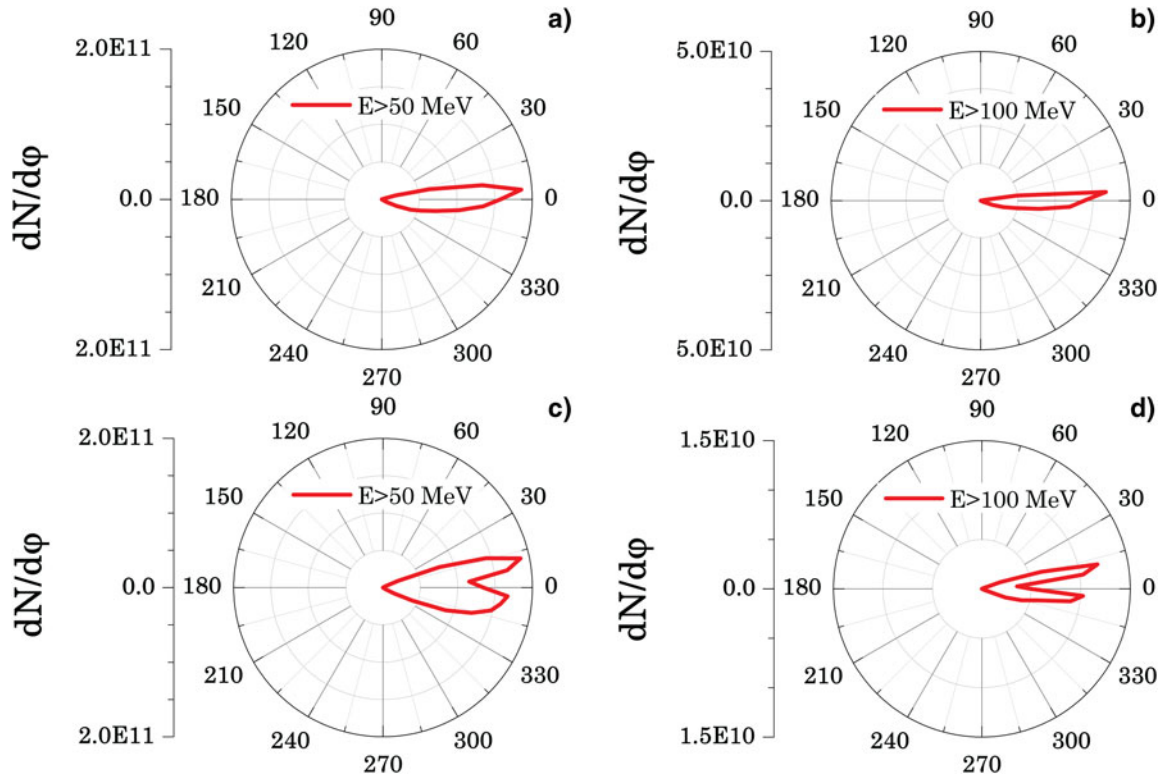

Fig. 8. Angular distributions of accelerated electrons with energies > 50 MeV [left, (a) and (c)] and >100 MeV [right, (b) and (d)] for preplasma scale lengths $L_r = 20$ [upper plots, (a) and (b)] and 1.8 μm [lower plots, (c) and (d)]. The laser pulse is *P*-polarized (along the *y*-axis) with the angle of incidence $\theta = 80°$, $\varphi = \arctan(p_y/p_x)$, where p_x and p_y are the electron momentum components.

length preplasma corona were analyzed in papers (Nakamura *et al*., 2004, 2007). In full agreement with 2D PIC simulation results of (Nakamura *et al*., 2007) (see Fig. 3 of this paper), the structure of quasi-static electric and magnetic fields obtained in our 3D PIC modeling (shown in Figure 9 for the preplasma scale length $L_r = 1.8$ μm) indicates the formation of the focusing electric and magnetic fields reflecting electrons towards the vacuum. It should be noted that the enhanced transverse momentum of accelerated electrons (see Fig. 8 for the preplasma scale lengths $L_r = 1.8$ μm), which exceeds substantially the normalized vector potential of the laser pulse, clearly indicates the resonant direct laser acceleration with assistance of quasi-static electric and magnetic fields (Pukhov *et al*., 1999).

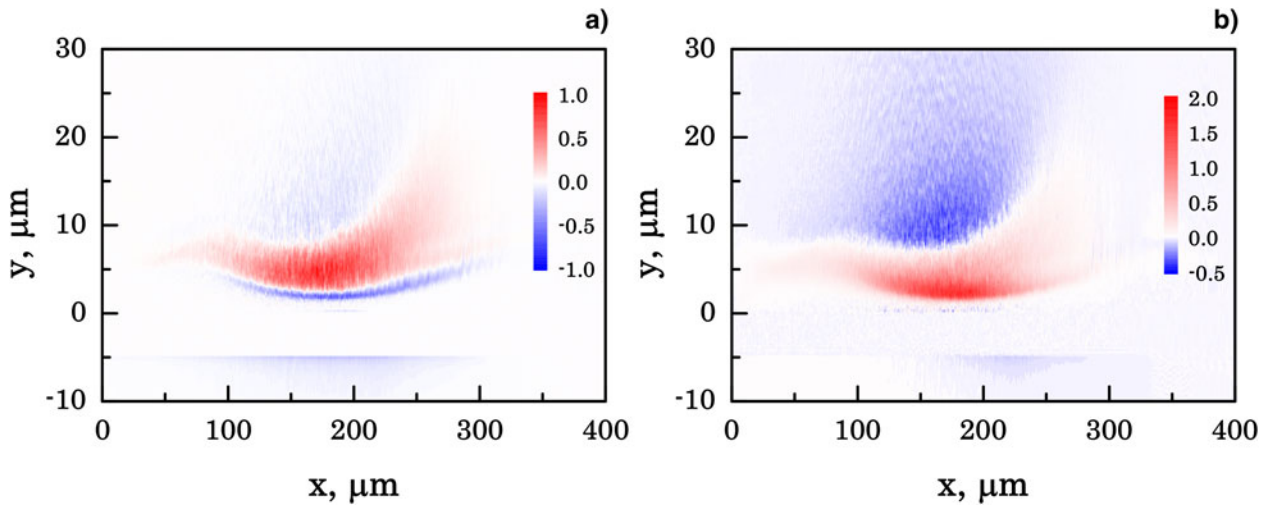

Fig. 9. Averaged over laser period electric field $\langle e_y \rangle \equiv \langle |e| E_y/mc\omega_0 \rangle$ – (a) and magnetic field $\langle b_z \rangle \equiv \langle |e| B_z/mc\omega_0 \rangle$ – (b) on the plane *OXY* at $z = 40$ μm, $ct = 200$ μm (when the laser pulse center is located at $x = 200$ μm) for the preplasma scale length $L_r = 1.8$ μm.

https://doi.org/10.1017/S0263034615001032 Published online by Cambridge University Press

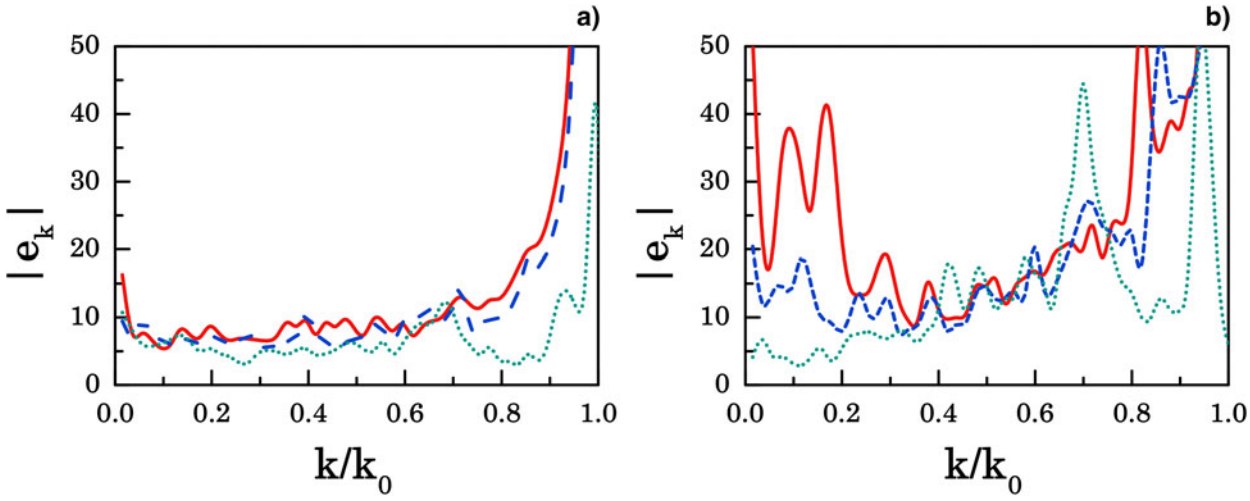

Fig. 10. Absolute value of the longitudinal electric field $e_x \equiv |e| E_x/mc\omega_0$ Fourier-component at time $ct = 200$ μm (when the laser pulse center is located at $x = 200$ μm) calculated for different intervals over OX: $x \in (0, 200)$ μm – (a) and $x \in (200, 400)$ μm – (b) for the different distances y from the initial target surface ($y = 0$): $y = 12$ μm – solid (red) curves, $y = 20$ μm – dashed (blue) curves, $y = 50$ μm – dotted (green) curves. Results presented for the preplasma scale length $L_r = 20$ μm and the laser incidence angle 80°.

A relatively low contrast nanosecond pedestal of the laser pulse can produce longer preplasma corona extended to tens of microns with density scales of the order or in excess of the laser spot size. In this case the mechanism of the laser acceleration along the target surface can be attributed to stochastic electron acceleration in plasma waves driven by an intense laser pulse at grazing incidence [see (Bochkarev *et al.*, 2014) and references cited therein]. Plasma waves in subcritical plasma are excited by a subpicosecond laser pulse with the duration much longer than the plasma wave period in the process of the pulse self-modulation (Antonsen & Mora, 1993; Krall *et al.*, 1993; Andreev *et al.*, 1996, 1992). The self-modulation instability develops from the front of the laser pulse and saturates due to the plasma wave breaking. Fourier spectra of the longitudinal electric field $e_x \equiv |e| E_x/mc\omega_0$ in the regions $x \in (0, 200)$ μm and $x \in (200, 400)$ μm, where the rear and front parts of the laser pulse are situated at $ct = 200$ μm, are shown in Figure 10(a) and 10(b), respectively, for the preplasma scale length $L_r = 20$ μm at different distances from the initial target surface.

The enhanced Fourier-component on the right plot of Figure 10 in the spectral range $k/k_0 \cong 0.1 \div 0.2$ ($k_0 = \omega_0/c$) reflects the excitation of plasma waves at plasma densities $n_e/n_{cr} \cong (1 \div 3) \times 10^{-2}$ that is just about and below the unperturbed laser reflection point ($y_r \approx 20$ μm) for the angle of incidence 80°. The absence of these spectral lines in the left plot of Figure 10 (for the rear part of the laser pulse) indicates the saturation of self-modulation instability and transmission of the excited plasma waves energy to accelerated electrons.

Angular distributions of fast electrons emitted from intense laser–solid interactions were investigated in experiments at the PHELIX laser system at Gesellschaft fur Schwerionenforschung, Darmstadt for different angles of laser incidence (Gray *et al.*, 2011). In these experiments the intensity contrast up to 50 ps prior to the peak of the pulse was about 10^{-6}, that corresponds to the long scale plasma corona of tens of microns (see Fig. 3, L_r). The measured angular distributions of energetic electrons for the laser incidence angle 80° is in good agreement with the modeling result shown in the upper plots of Figure 8.

In conclusion, preplasma formation under the action of different contrast prepulses is modeled and described using the wide-range two-temperature hydrodynamic model. The preplasma density profiles for different contrast ratios of the nanosecond pedestal are found and used as the initial density distributions in 3D PIC simulations of electron acceleration by the main P-polarized laser pulse.

The generation of hot electrons at the grazing incidence of a subpicosecond relativistic-intense laser pulse onto the plane solid target is analyzed for the parameters typical for petawatt class laser systems. Table 1 summarizes the parameters of

Table 1. *The parameters of electrons accelerated to high energies for two typical scale lengths of the preplasma density.*

Preplasma density scale length L_r, (μm)	Percent of the laser energy transmitted to electrons η with energies >0.5 MeV	Percent of the laser energy transmitted to electrons η with energies >1.5 MeV	Charge of electrons Q accelerated to energies >50 MeV	Charge of electrons Q accelerated to energies >100 MeV
$L_r = 1.8$ μm	η = 7.0%	η = 6.8%	$Q = 21.7$ nC	$Q = 0.9$ nC
$L_r = 20$ μm	η = 8.5%	η = 7.1%	$Q = 11.8$ nC	$Q = 1.9$ nC

https://doi.org/10.1017/S0263034615001032 Published online by Cambridge University Press

electrons accelerated to high energies for two typical scale lengths of the preplasma density $L_r = 1.8$ and 20 μm. For the grazing incidence of the laser pulse, the substantial increase of the characteristic energy, number, and collimation of electrons accelerated along the target surface is demonstrated (see Figs 5–7) in comparison with the ponderomotive scaling of laser–target interaction (Wilks *et al*., 1992; Chen *et al*., 2009).

ACKNOWLEDGMENTS

This work was supported by the Russian Science Foundation grant 14-50-00124.

REFERENCES

Andreev, N.E., Gorbunov, L.M., Kirsanov, V., Pogosova, A.A. & Ramazashvili, R.R. (1992). Resonant excitation of wakefields by a laser pulse in a plasma. *JETP Lett*. **55**, 6.

Andreev, N.E., Gorbunov, L.M., Kirsanov, V.I., Pogosova, A.A. & Sakharov, A.S. (1996). Theory of the resonance modulational instability of short laser pulses in a homogeneous plasma and plasma channels. *Plasma Phys. Rep*. **22**, 379–389.

Andreev, N.E., Povarnitsyn, M.E., Veysman, M.E., Faenov, A.Y., Levashov, P.R., Khishchenko, K.V., Pikuz, T.A., Magunov, A.I., Rosmej, O.N., Blazevic, A., Pelka, A., Schaumann, G., Schollmeier, M. & Roth, M. (2015). Interaction of annular-focused laser beams with solid targets. *Laser Part. Beams* **33**, 541–550.

Antonsen Jr., T. & M. Mora, P. (1993). Self-focusing and Raman scattering of laser pulses in tenuous plasmas. *Phys. Fluids B* **5**, 1440–1452.

Bagnoud, V., Aurand, B., Blazevic, A., Borneis, S., Bruske, C., Ecker, B., Eisenbarth, U., Fils, J., Frank, A., Gaul, E., Goette, S., Haefner, C., Hahn, T., Harres, K., Heuck, H.-M., Hochhaus, D., Hoffmann, D.H.H., Javorková, D., Kluge, H.-J., Kuehl, T., Kunzer, S., Kreutz, M., Merz-Mantwill, T., Neumayer, P., Onkels, E., Reemts, D., Rosmej, O., Roth, M., Stoehlker, T., Tauschwitz, A., Zielbauer, B., Zimmer, D. & Witte, K. (2010). Commissioning and early experiments of the phelix facility. *Appl. Phys. B* **100**, 137–150.

Bochkarev, S.G., Brantov, A.V., Bychenkov, V.Y., Torshin, D.V., Kovalev, V.F., Baidin, G.V. & Lykov, V.A. (2014). Stochastic electron acceleration in plasma waves driven by a high-power subpicosecond laser pulse. *Plasma Phys. Rep*. **40**, 202–214.

Brabetz, C., Busold, S., Cowan, T., Deppert, O., Jahn, D., Kester, O., Roth, M., Schumacher, D. & Bagnoud, V. (2015). Laser-driven ion acceleration with hollow laser beams. *Phys. Plasmas* **22**, 013105.

Chen, H., Wilks, S.C., Kruer, W.L., Patel, P.K. & Shepherd, R. (2009). Hot electron energy distributions from ultraintense laser solid interactions. *Phys. Plasmas* **16**, 020705.

Esirkepov, T.Z., Koga, J.K., Sunahara, A., Morita, T., Nishikino, M., Kageyama, K., Nagatomo, H., Nishihara, K., Sagisaka, A., Kotaki, H., Nakamura, T., Fukuda, Y., Okada, H., Pirozhkov, A.S., Yogo, A., Nishiuchi, M., Kiriyama, H., Kondo, K., Kando, M. & Bulanov, S.V. (2014). Prepulse and amplified spontaneous emission effects on the interaction of a petawatt class laser with thin solid targets. *Nucl. Instrum. Methods A* **745**, 150–163.

Gray, R.J., Yuan, X.H., Carroll, D.C., Brenner, C.M., Coury, M., Quinn, M.N., Tresca, O., Zielbauer, B., Aurand, B., Bagnoud, V., Fils, J., Kгјhl, T., Lin, X.X., Li, C., Li, Y.T., Roth, M., Neely, D. & McKenna, P. (2011). Surface transport of energetic electrons in intense picosecond laser-foil interactions. *Appl. Phys. Lett*. **99**, 171502.

Krall, J., Ting, A., Esarey, E. & Sprangle, P. (1993). Enhanced acceleration in a self-modulated-laser wake-field accelerator. *Phys. Rev. E* **48**, 2157.

Mao, J.Y., Chen, L.M., Huang, K., Ma, Y., Zhao, J.R., Li, D.Z., Yan, W.C., Ma, J.L., Aeschlimann, M., Wei, Z.Y. & Zhang, J. (2015). Highly collimated monoenergetic target-surface electron acceleration in near-critical-density plasmas. *Appl. Phys. Lett*. **106**, 131105.

Morace, A., Fedeli, L., Batani, D., Baton, S., Beg, F.N., Hulin, S., Jarrott, L.C., Margarit, A., Nakai, M., Nakatsutsumi, M., Nicolai, P., Piovella, N., Wei, M.S., Vaisseau, X., Volpe, L. & Santos, J.J. (2014). Development of X-ray radiography for high energy density physics. *Phys. Plasmas* **21**, 102712.

Nakamura, T., Kato, S., Nagatomo, H. & Mima, K. (2004). Surface-magnetic-field and fast-electron current-layer formation by ultraintense laser irradiation. *Phys. Rev. Lett*. **93**, 265002.

Nakamura, T., Mima, K., Sakagami, H. & Johzaki, T. (2007). Electron surface acceleration on a solid capillary target inner wall irradiated with ultraintense laser pulses. *Phys. Plasmas* **14**, 053112.

Ortner, A., Faik, S., Schumacher, D., Basko, M.M., Blazevic, A., Busold, S., Bedacht, S., Cayzac, W., Frank, A., Kraus, D., Rienecker, T., Schaumann, G., Tauschwitz, A., Wagner, F. & Roth, M. (2015). A novel double hohlraum target to create a moderately coupled plasma for ion stopping experiments. *Nucl. Instrum. Methods B* **343**, 123–131.

Povarnitsyn, M.E., Andreev, N.E., Apfelbaum, E.M., Itina, T.E., Khishchenko, K.V., Kostenko, O.F., Levashov, P.R. & Veysman, M.E. (2012*a*). A wide-range model for simulation of pump-probe experiments with metals. *Appl. Surf. Sci*. **258**, 9480–9483.

Povarnitsyn, M.E., Andreev, N.E., Levashov, P.R., Khishchenko, K.V., Kim, D.A., Novikov, V.G. & Rosmej, O.N. (2013). Laser irradiation of thin films: Effect of energy transformation. *Laser Part. Beams* **31**, 663–671.

Povarnitsyn, M.E., Andreev, N.E., Levashov, P.R., Khishchenko, K.V. & Rosmej, O.N. (2012*b*). Dynamics of thin metal foils irradiated by moderate-contrast high-intensity laser beams. *Phys. Plasmas* **19**, 023110.

Pukhov, A. (1999). Three-dimensional electromagnetic relativistic particle-in-cell code VLPL (Virtual Laser Plasma Lab). *J. Plasma Phys*. **61**, 425–433.

Pukhov, A., Sheng, Z.-M. & Meyer-ter Vehn, J. (1999). Particle acceleration in relativistic laser channels. *Phys. Plasmas* **6**, 2847–2854.

Rusby, D.R., Wilson, L.A., Gray, R.J., Dance, R.J., Butler, N.M.H., MacLellan, D.A., Scott, G.G., Bagnoud, V., Zielbauer, B., McKenna, P. & Neely, D. (2015). Measurement of the angle, temperature and flux of fast electrons emitted from intense laser–solid interactions. *J. Plasma Phys*. **81**, 475810505.

Schollmeier, M., Sefkow, A.B., Geissel, M., Arefiev, A.V., Flippo, K.A., Gaillard, S.A., Johnson, R.P., Kimmel, M.W., Offermann, D.T., Rambo, P.K., Schwarz, J. & Shimada, T. (2015).

https://doi.org/10.1017/S0263034615001032 Published online by Cambridge University Press

Laser-to-hot-electron conversion limitations in relativistic laser matter interactions due to multi-picosecond dynamics. *Phys. Plasmas* **22**, 043116.

Vaisseau, X., Debayle, A., Honrubia, J.J., Hulin, S., Morace, A., Nicola, P., Sawada, H., Vauzour, B., Batani, D., Beg, F.N., Davies, J.R., Fedosejevs, R., Gray, R.J., Kemp, G.E., Kerr, S., Li, K., Link, A., McKenna, P., McLean, H.S., Mo, M., Patel, P.K., Park, J., Peebles, J., Rhee, Y.J., Sorokovikova, A., Tikhonchuk, V.T., Volpe, L., Wei, M. & Santos, J.J. (2015). Enhanced relativistic-electron-beam energy loss in warm dense aluminum. *Phys. Rev. Lett*. **114**, 095004.

Wagner, F., Bedacht, S., Ortner, A., Roth, M., Tauschwitz, A., Zielbauer, B. & Bagnoud, V. (2014*a*). Pre-plasma formation in experiments using petawatt lasers. *Opt. Express* **22**, 29505–29514.

Wagner, F., João, C., Fils, J., Gottschall, T., Hein, J., Körner, J., Limpert, J., Roth, M., Stöhlker, T. & Bagnoud, V. (2014*b*). Temporal contrast control at the phelix petawatt laser facility by means of tunable sub-picosecond optical parametric amplification. *Appl. Phys. B* **116**, 429–435.

Wang, W.M., Chen, L.M., Mao, J.Y., Huang, K., Ma, Y., Zhao, J.R., Zhang, L., Yan, W.C., Li, D.Z., Ma, J.L., Ly, Y.T., Lu, X., Wei, Z.Y., Sheng, Z.M. & Zhang, J. (2013). Collimated quasi-monoenergetic electron beam generation from intense laser solid interaction. *High Energy Density Phys*. **9**, 578–582.

Wilks, S.C., Kruer, W.L., Tabak, M. & Langdon, A.B. (1992). Absorption of ultra-intense laser pulses. *Phys. Rev. Lett*. **69**, 1383.

https://doi.org/10.1017/S0263034615001032 Published online by Cambridge University Press